Letter Editors' Suggestion

Massive Dirac fermions in moiré superlattices: A route towards topological flat minibands and correlated topological insulators

Ying Su,[1,2] Heqiu Li,[3,4] Chuanwei Zhang,[2] Kai Sun,[3] and Shi-Zeng Lin[1]

[1]*Theoretical Division, T-4 and CNLS, Los Alamos National Laboratory, Los Alamos, New Mexico 87545, USA*
[2]*Department of Physics, The University of Texas at Dallas, Richardson, Texas 75080, USA*
[3]*Department of Physics, University of Michigan, Ann Arbor, Michigan 48109, USA*
[4]*Department of Physics, University of Toronto, Toronto, Ontario M5S 1A7, Canada*

(Received 6 October 2021; revised 20 June 2022; accepted 26 July 2022; published 12 August 2022)

We demonstrate a generic mechanism to realize topological flat minibands by confining massive Dirac fermions in a periodic moiré potential, which can be achieved in a heterobilayer of transition metal dichalcogenides. We show that the topological phase can be protected by the symmetry of moiré potential and survive to arbitrarily large Dirac band gap. We take the $MoTe_2/WSe_2$ heterobilayer as an example and find that the topological phase can be driven by a vertical electric field. By projecting the Coulomb interaction onto the topological fat minibands, we identify a correlated Chern insulator at half filling and a quantum valley-spin Hall insulator at full filling which explains the topological states observed in the $MoTe_2/WSe_2$ in the experiment. Our work clarifies the importance of Dirac structure for the topological minibands and unveils a general strategy to design topological moiré materials.

DOI: 10.1103/PhysRevResearch.4.L032024

Introduction.—Electrons confined by periodic potential in a crystal can behave very differently from a free particle. Perhaps the most prominent example is graphene in which the timereversal, inversion, and threefold rotation symmetries together stabilize a pair of Dirac cones at Brillouin zone corners [1]. The massless Dirac fermion (DF) can acquire a mass when the timereversal or inversion symmetry is broken, like in transition metal dichalcogenide (TMD) [2,3]. The nontrivial topological properties associated with the exotic quasiparticles enable novel quantum effects such as the Klein tunneling [4], valley Hall effect [5,6], and valley-selective circular dichroism [3,7,8] in these 2D materials which are considered candidates for the next-generation microelectronics.

When overlapping these 2D materials, the moiré superlattices (MSL) formed by misalignment open a new possibility to confine DF in a periodic moiré potential generated by interlayer hybridization and lattice corrugation. Recently, the topological flat minibands identified in twisted multilayer graphene [9–27], ABC-stacked-trilayer graphene/hBN heterostructure [28–30], and TMD homobilayer [31] have evoked great interest because the interplay between electronic correlation and nontrivial topology can stabilize exotic quantum states including unconventional superconductivity [32–62] and fractional Chern insulator [63–67].

TMD heterobilayers are another important class of MSL and are being considered as platforms to simulate the Hubbard model. Their single-particle physics is modeled by holes with parabolic dispersion subject to a moiré potential that yields topologically trivial moiré minibands [68,69]. In this approach, the massive Dirac structure of TMD is neglected by perturbatively dropping the conduction (remote) band, which is far away from the Fermi energy (of the order of 1eV). This theoretical framework can describe the experimentally observed Mott insulator and Wigner crystal in the WSe_2/WS_2 heterobilayer [70–75].

Strikingly, recent experiments report the correlated Chern insulator (CCI) at half filling ($\nu = 1$ hole per moiré unit cell) and quantum valley-spin Hall insulator (QVSHI) at full filling ($\nu = 2$ holes per moiré unit cell) in an AB-stacked $MoTe_2/WSe_2$ heterobilayer under a vertical electric field [76]. The experimental observations suggest valley-contrasting Chern bands in the TMD heterobilayer that cannot be explained by the existing model [68,69]. This motivates us to investigate a general problem that whether massive DF confined in a moiré potential can give rise to topological minibands.

In this Letter, we study the behavior of massive DF in a moiré potential. Surprisingly, we show that, no matter how large the Dirac band gap is, topological flat minibands can emerge when the moiré potential has certain symmetries. Our study indicates that the Dirac nature of electrons plays a crucial role in determining the topology of moiré minibands. In particular, we find that the Berry curvature induced by Dirac remote bands stabilizes an intrinsic topological phase, which is absent if remote bands are ignored. By applying our model to the $MoTe_2/WSe_2$ heterobilayer, we demonstrate that the Coulomb interaction can stabilize a CCI at $\nu = 1$ and a QVSHI at $\nu = 2$ in a vertical electric field, which agrees with the recent experiment [76]. Furthermore, the potential realizations of our model on the surface of an axion insulator and in a monolayer TMD under spatially periodic modulation are also proposed. Therefore, our work unveils a general route towards topological flat minibands in moiré systems.

Model.—The continuum model describing a massive DF in a moiré potential reads

$$H_\tau = h_{\boldsymbol{k},\tau} + V(\boldsymbol{r}), \quad h_{\boldsymbol{k},\tau} = v_F(\tau k_x\sigma_x + k_y\sigma_y) + m\sigma_z, \quad (1)$$

where v_F is the Fermi velocity, m is the Dirac mass, and $\sigma_{x,y,z}$ are the Pauli matrices acting on pseudospin. $\tau = \pm 1$ determines the chirality of the massive DF and is dubbed valley index in TMD [3]. The Dirac Hamiltonian $h_{\boldsymbol{k},\tau}$ yields a massive Dirac cone $E_{\pm,\boldsymbol{k}} = \pm\sqrt{v_F^2\boldsymbol{k}^2 + m^2}$ with a direct band gap $\Delta = 2m$. Here we consider the moiré potential $V(\boldsymbol{r}) = 2V_0\sum_{j=1}^{3}\cos(\boldsymbol{G}_j\cdot\boldsymbol{r} + \phi)$ in TMD heterobilayers [68,69], where $\boldsymbol{G}_j = \frac{4\pi}{\sqrt{3}a_M}(\cos\frac{2\pi j}{3}, \sin\frac{2\pi j}{3})$ and a_M is the MSL constant. H_τ is invariant under the threefold rotation since $\mathcal{C}_3 h_{\boldsymbol{k},\tau}\mathcal{C}_3^{-1} = h_{R_3\boldsymbol{k},\tau}$ and $V(R_3\boldsymbol{r}) = V(\boldsymbol{r})$ where $\mathcal{C}_3 = \mathrm{diag}(e^{-\frac{2\pi\tau i}{3}}, 1)$ [77] and R_3 are the threefold rotation operator and matrix.

As far as the energy spectrum is concerned, the massive DF described by $h_{\boldsymbol{k},\tau}$ can be approximated by a free fermion with effective mass $m^* = \Delta/2v_F^2$ through the second order perturbation theory when the Dirac band gap $\Delta \gg v_F|\boldsymbol{k}|$ and V_0. Then Eq. (1) is reduced to

$$H_0 = -\frac{\boldsymbol{k}^2}{2m^*} + V(\boldsymbol{r}), \quad (2)$$

which is widely adopted to describe the moiré minibands in TMD heterobilayers [68,69]. However, as will be shown explicitly below, the topology of minibands can be very different for Eqs. (1) and (2) because H_0 has time-reversal symmetry (TRS) while H_τ does not. The TRS in H_τ is broken by the massive DF; i.e., $\mathcal{T}h_{\boldsymbol{k},\tau}\mathcal{T}^{-1} = h_{-\boldsymbol{k},-\tau}$ where the TRS operator $\mathcal{T} = \mathcal{K}$ equals the complex conjugate operator $\mathcal{K}$. Therefore, the topological moiré minibands can emerge from Eq. (1) but not Eq. (2).

Topological phases.—Due to the $\mathcal{C}_3$ symmetry of H_τ, the Chern number C_τ of the moiré miniband can be determined by its $\mathcal{C}_3$ eigenvalues $\eta_\tau(\boldsymbol{k})$ at the $\mathcal{C}_3$-invariant points [78]

$$e^{\frac{2\pi i}{3}C_\tau} = \eta_\tau(\gamma)\eta_\tau(\kappa)\eta_\tau(-\kappa), \quad (3)$$

where γ represents the moiré Brillouin zone (MBZ) center and $\pm\kappa$ are the MBZ corners. Here we focus on the top valence band. It is easy to show $\eta_\tau(\gamma) = 1$, while $\eta_\tau(\pm\kappa)$ can be evaluated to the leading order by the degenerate perturbation theory in which the coupling among three degenerate Bloch states at $\pm\kappa_{1,2,3}$ are considered, as shown in Fig. 1(a). In the basis of the Bloch states of the valence band without a moiré potential, i.e., $\{|u_{\pm\kappa_1,\tau}\rangle, |u_{\pm\kappa_2,\tau}\rangle, |u_{\pm\kappa_3,\tau}\rangle\}$ with $h_{\boldsymbol{k},\tau}|u_{\boldsymbol{k},\tau}\rangle = -\sqrt{v_F^2\boldsymbol{k}^2 + m^2}\,|u_{\boldsymbol{k},\tau}\rangle$, the matrix representation of the moiré potential operator is

$$V_{\pm\kappa,+} = V^*_{\mp\kappa,-} = \begin{pmatrix} 0 & w(\pm\phi) & w(\pm\phi)^* \\ w(\pm\phi)^* & 0 & w(\pm\phi) \\ w(\pm\phi) & w(\pm\phi)^* & 0 \end{pmatrix}, \quad (4)$$

whose matrix element $w(\pm\phi) = \langle u_{\pm\kappa_1,+}|V|u_{\pm\kappa_2,+}\rangle = V_0 e^{i(\pm\phi - \frac{\pi}{3})}(\frac{1}{2} + \frac{i\sqrt{3}}{2\sqrt{1+s}})$ depends on the dimensionless parameter $s = 64\pi^2 v_F^2/9\Delta^2 a_M^2$. Interestingly, s is proportional to the intrinsic Berry curvature $\Omega_I(\boldsymbol{k}) \approx 2v_F^2/\Delta^2$ of massive DF (which is valid for $\Delta \gg at|\boldsymbol{k}|$ in the MBZ) times the MBZ area $A_M = 8\pi^2/\sqrt{3}a_M^2$.

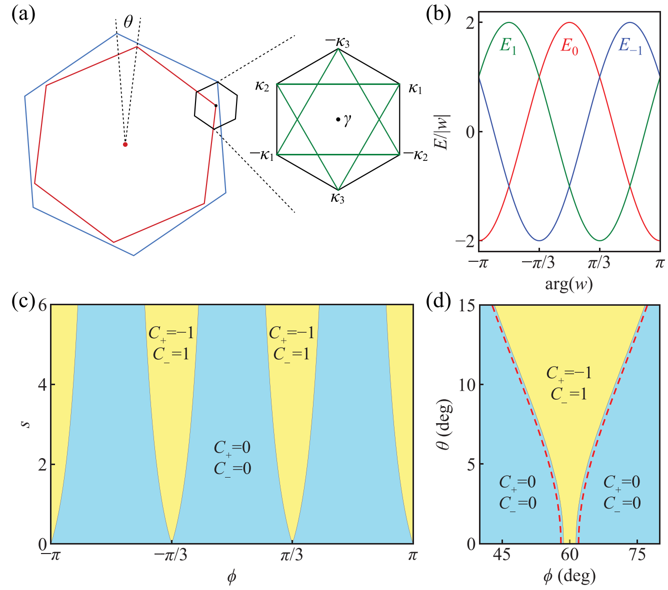

FIG. 1. (a) Schematic MBZ in a TMD heterobilayer. The MBZ center is shifted to be coincident with the +K valley of the active layer. The green lines denote the coupling among three degenerate Bloch states at MBZ corners. (b) Eigenvalues of Eq. (4) as a function of arg(w). (c) Topological phase diagram of the continuum model Eq. (1) in terms of ϕ and s. (d) Topological phase diagram of the $MoTe_2/WSe_2$ heterobilayer in terms of ϕ and θ. The yellow (blue) regions are the topological (trivial) phase with valley Chern numbers $C_\pm = \mp 1$ ($C_\pm = 0$). The red dashed lines in (d) are the topological phase boundaries predicted by Eq. (5).

The eigenvalues of Eq. (4) are $E_0 = 2\mathrm{Re}(w)$ and $E_{\pm 1} = -\mathrm{Re}(w) \pm \sqrt{3}\mathrm{Im}(w)$, and the corresponding eigenstates have the $\mathcal{C}_3$ eigenvalues $\mathcal{C}_3|E_j\rangle = e^{i\frac{2\pi j}{3}}|E_j\rangle$. In Fig. 1(b), the three eigenvalues are shown as a function of arg(w) and the top valence band at $\pm\kappa$ changes among E_0 and $E_{\pm 1}$ through the band crossing at $\arg(w) = (2n+1)\pi/3$ with $n \in \mathbb{Z}$ where the topological transition can occur. In this way, we can identify $\eta_\tau(\pm\kappa)$ and hence the valley Chern number C_τ according to Eq. (3). Moreover, the TRS guarantees $\eta_+(\pm\kappa) = \eta_-(\mp\kappa)^*$ and $C_+ = -C_-$. A global phase diagram in terms of ϕ and s is constructed in Fig. 1(c). The topological phases with $C_\pm = \mp 1$ emerge at $\phi = (2n+1)\pi/3$ and then expand in a wider range of ϕ as s increases from zero. This indicates that the intrinsic Berry curvature of massive DF measured by s plays a crucial role in determining the topology of moiré minibands. The topological phase boundaries can be obtained analytically by demanding $\arg[w(\pm\phi)] = (2n+1)\pi/3$ that yields

$$s = 3\cot^2\left(\phi - \frac{2n\pi}{3}\right) - 1, \quad (5)$$

with $\phi \in [(2n-1)\pi/3, (2n+1)\pi/3]$.

Significantly, the topological phases at $\phi = (2n+1)\pi/3$ persist to arbitrarily large Dirac band gap since $s \to 0$ when $\Delta \to \infty$, as shown in Fig. 1(c). To understand the peculiar behavior, it is noticed that the moiré potential minima for holes form a honeycomb lattice with inversion symmetry $\mathcal{P}$ only at

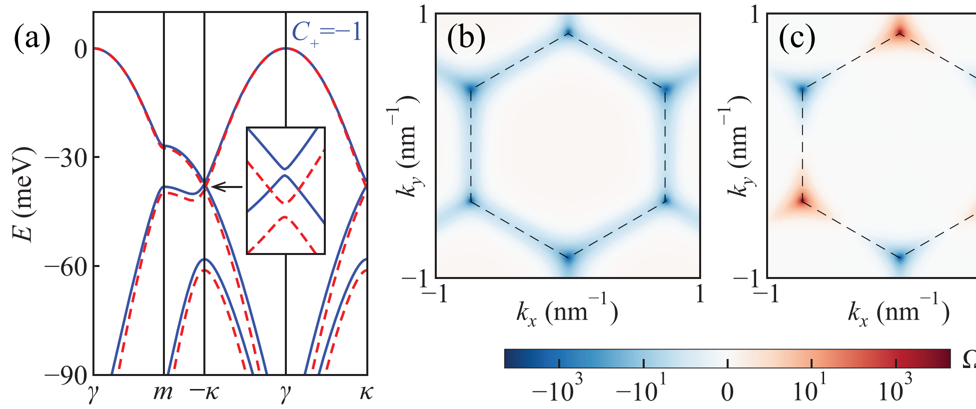

FIG. 2. (a) Valence bands of the $MoTe_2/WSe_2$ heterobilayer with $\theta = 1^\circ$, $\phi = 59^\circ$, and $V_0 = 8$ meV. The blue solid and red dashed bands are from the continuum models in Eqs. (1) and (2), respectively. (b) and (c) Berry curvatures of the top blue and red bands in (a). The black dashed hexagon encloses the MBZ.

these ϕs. Then free fermions coupled to the moiré potential, as described by Eq. (2), give rise to a pair of Dirac cones at MBZ corners that is stabilized by the $\mathcal{PT}$ and $\mathcal{C}_3$ symmetries, same as that in graphene. When the free fermion is replaced by massive DF in Eq. (1), the $\mathcal{PT}$ symmetry is broken as $\mathcal{PT}h_{\boldsymbol{k},\tau}(\mathcal{PT})^{-1} = h_{\boldsymbol{k},-\tau}$ that gaps out the Dirac cones and leads to topological minibands. This mechanism to generate topological minibands is protected by the symmetry of moiré potential and is independent on the detailed model parameters. The derivation of ϕ from $(2n+1)\pi/3$ breaks the $\mathcal{P}$ symmetry and induces a staggered potential on the honeycomb lattice that can drive the topological transition as in the Haldane model [79]. When $\phi = 2n\pi/3$, the moiré potential also has $\mathcal{P}$ symmetry but its minima for holes form a triangular lattice that leads to a trivial top valence band [80].

$MoTe_2/WSe_2$ *heterobilayer.*—To verify the topological phase, we take the $MoTe_2/WSe_2$ heterobilayer as an example. $MoTe_2/WSe_2$ has the type-I band alignment with a valence band offset about 200 to300 meV. The valence band maximum is from $MoTe_2$ whose Fermi velocity is $v_F = 2.526$ eV Å and Dirac band gap is $\Delta = 1.017$ eV [81]. The lattice mismatch is $\delta \sim 7\%$ that results in a MSL with $a_M = a/\sqrt{\delta^2+\theta^2}$ where θ is a twist angle and $a = 3.565$ Å is the lattice constant of $MoTe_2$ [82]. The direct interlayer tunneling is suppressed by the band offset and by the spin-valley locking in the AB-stacking pattern that requires flipping the electron spin. Therefore, the massive DF from $MoTe_2$ coupled to the moiré potential provided by WSe_2 can be described by Eq. (1). By employing the plane wave expansion of the continuum model, we obtain the topological phase diagram in terms of ϕ and θ in Fig. 1(d). Here the red dashed lines are the topological phase boundaries predicted by Eq. (5) and are consistent with the direct numerical calculation of Eq. (1). In Fig. 1(d), only the topological phase around $\phi = \pi/3$ is shown and other topological phases can be obtained by shifting ϕ by $2n\pi/3$.

To compare the moiré minibands for Eqs. (1) and (2), we choose $\theta = 1^\circ$ and $\phi = 59^\circ$ in the topological phase and set $V_0 = 8$ meV. In Fig. 2(a), the blue and red energy bands are from Eqs. (1) and (2), respectively, and show good agreement with each other. Here only the valence bands from the +K valley are plotted, and those from the −K valley can be obtained by TRS. The Berry curvature of the top blue band is shown in Fig. 2(b) and yields a valley Chern number $C_+ = -1$, while that of the top red band is antisymmetric in Fig. 2(c) due to the emergent TRS in Eq. (2). The Wannier orbitals of the moiré minibands and the trivial phases from different models are compared in the Supplemental Material [83].

Electric-field-driven topological transition.—According to the density functional theory (DFT) calculation, the phase of the moiré potential in AA- and AB-stacked TMD heterobilayer is unlikely close to $\phi \sim (2n+1)\pi/3$ [68,69,84]. Here we show that ϕ can be tuned by a vertical electric field. It is noted that the two stacking configurations have different lattice corrugations that have been identified in both the STM measurements [85,86] and DFT calculations [84,87]. The electric field couples to the lattice corrugation and modifies the moiré potential as

$$\begin{aligned} H'_\tau &= h_{\boldsymbol{k},\tau} + V(\boldsymbol{r}) + eE_\perp z(\boldsymbol{r}) \\ &= h_{\boldsymbol{k},\tau} + 2V'_0 \sum_{j=1}^{3} \cos\left(\boldsymbol{G}_j\cdot\boldsymbol{r} + \frac{\phi+\phi'}{2} + \beta\right), \end{aligned} \tag{6}$$

where $E_\perp$ is the vertical electric field and the topography of the corrugated layer is approximated by the lowest harmonics $z(\boldsymbol{r}) \approx z_0 \sum_{j=1}^{3} \cos(\boldsymbol{G}_j\cdot\boldsymbol{r} + \phi')$. The role of electric field can be described by a modified moiré potential with $V'_0 = \sqrt{V_0^2 + e^2E_\perp^2 z_0^2/4 + V_0 eE_\perp z_0 \cos(\phi-\phi')}$ and $\tan\beta = \frac{2V_0 - eE_\perp z_0}{2V_0 + eE_\perp z_0}\tan(\frac{\phi-\phi'}{2})$. As $E_\perp$ ramps up, the phase of the moiré potential in Eq. (6) changes continuously from ϕ to ϕ' when $eE_\perp z_0 \gg V_0$, which points to an electric-field-driven topological phase transition.

In the AA-stacked TMD heterobilayer, $z(\boldsymbol{r})$ is maximal at R_M^M and minimal at R_X^M and R_M^X [85–87]. In the AB-stacked TMD heterobilayer, $z(\boldsymbol{r})$ is maximal (minimal) at R_X^X (R_X^M), while H_M^M is in between [84,86]. Here M and X refer to the metal and chalcogen, while R and H represent the AA- and AB-stacking. The super- and subscript denote atoms from the top and bottom layer that are aligned locally [83]. The variation of $z(\boldsymbol{r})$ in experiments translates into $\phi' \sim 0$ and $-\pi/2$ for the AA- and AB-stacked heterobilayer, as shown in Figs. 3(a) and 3(b). ϕ of the moiré potential is usually determined by fitting the continuum model to the DFT energy bands. It has been reported that $\phi \sim \pi/12$ for AB-stacked $MoTe_2/WSe_2$

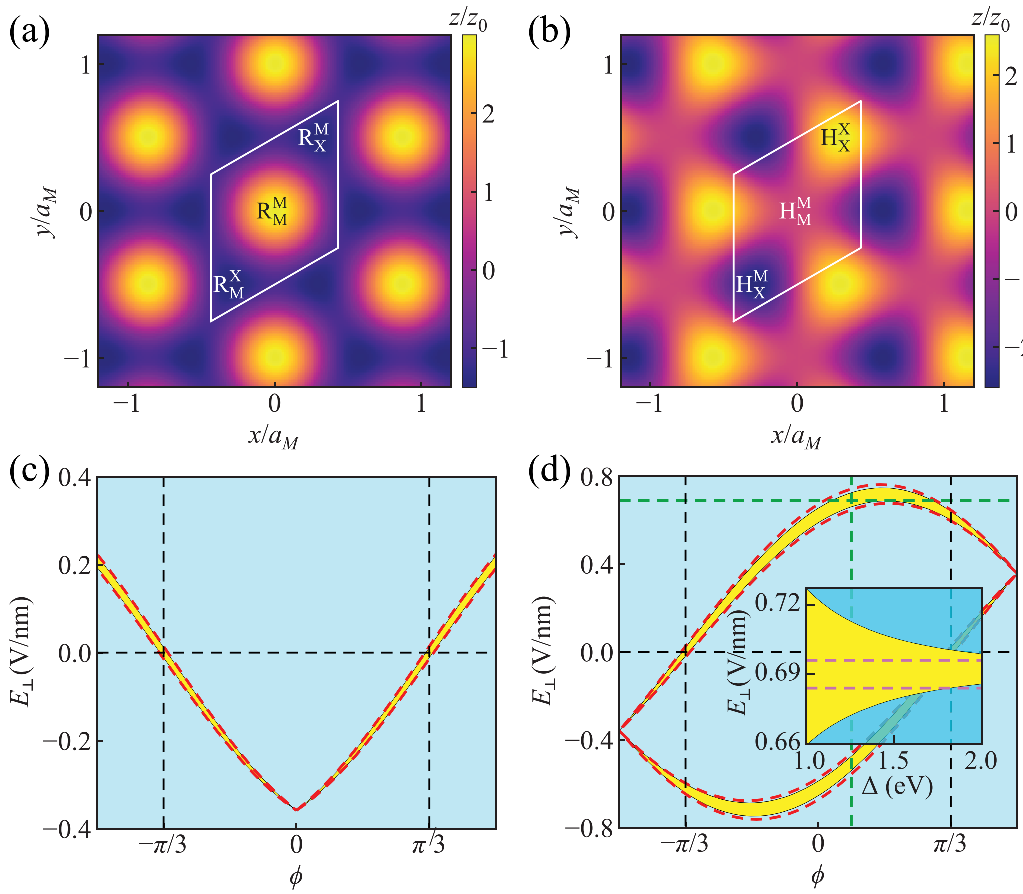

FIG. 3. (a) and (b) Topography of the corrugated AA- and AB-stacked TMD heterobilayer. The white parallelogram encloses the moiré unit cell. (c) and (d) Topological phase diagrams of the AA- and AB-stacked $MoTe_2/WSe_2$ heterobilayer in terms of ϕ and $E_\perp$. The yellow (blue) regions are the topological (trivial) phase with valley Chern numbers $C_\pm = \mp 1$ ($C_\pm = 0$). The red dashed lines are the topological phase boundaries predicted by Eq. (5). The green dashed lines in (d) are for $\phi = \pi/12$ and $E_\perp = 0.69$ V/nm. The inset of (d) shows the change of topological phase at $\phi = \pi/12$ vs Δ and the two dash lines are the upper and lower critical electric fields extracted from Ref. [76].

[84] while ϕ for AA-stacked $MoTe_2/WSe_2$ is still unclear. Nevertheless, most AA-stacked TMD heterobilayers have a ϕ of $\pi/6 \sim \pi/4$ [69,88] and it is natural to expect AA-stacked $MoTe_2/WSe_2$ has ϕ in the same range. The critical $E_\perp$ for the topological transition can be obtained from Eq. (5) by replacing ϕ with the phase of the modified moiré potential in Eq. (6). For $\theta = 0^\circ$, $V_0 = 4.3$ meV, and $z_0 = 0.024$ nm, the topological phase diagrams in terms of ϕ and $E_\perp$ are displayed in Figs. 3(c) and 3(d) for AA- and AB-stacked $MoTe_2/WSe_2$, respectively. The former shows a topological phase for ϕ around $\pi/6 \sim \pi/4$ in negative $E_\perp$, while the latter exhibits two topological phases for $\phi \sim \pi/12$ in both positive and negative $E_\perp$. Note that the positive (negative) $E_\perp$ reduces (enlarges) the valence band offset and is applied in the experiment. Therefore, we can focus on $E_\perp > 0$ and there is no topological phase for AA-stacked $MoTe_2/WSe_2$ as observed in the experiment [89]. For AB-stacked $MoTe_2/WSe_2$, a topological phase appears for $E_\perp$ within $0.66 \sim 0.73$ V/nm that agrees well with the experimental result of $0.68 \sim 0.70$ V/nm [76]. The Dirac gap could be underestimated by DFT calculations (for example, $\Delta = 1.72$ eV according to Ref. [90]). Our theory exhibits a reasonable agreement with the experimental data for a relevant range of Δ, as displayed in the inset of Fig. 3(d).

CCI and QVSHI.—To stabilize a Chern insulator, it is required to break the TRS, which can be achieved by the Coulomb interaction. The Coulomb interaction projected onto the moiré minibands reads

$$H = \sum_{n,\boldsymbol{k},\tau} (E_{n,\boldsymbol{k},\tau} - \mu) c^\dagger_{n,\boldsymbol{k},\tau} c_{n,\boldsymbol{k},\tau} + \frac{1}{2A} \sum_{\boldsymbol{q}} \rho(\boldsymbol{q}) V_{\boldsymbol{q}} \rho(-\boldsymbol{q}), \tag{7}$$

where $c_{n,\boldsymbol{k},\tau}$ is the annihilation operator of the eigenstate given by $H'_\tau |\psi_{n,\boldsymbol{k},\tau}\rangle = E_{n,\boldsymbol{k},\tau} |\psi_{n,\boldsymbol{k},\tau}\rangle$, A is the area of the system, and μ is the chemical potential. $V_{\boldsymbol{q}} = e^2 \tanh(q d_\perp)/2\epsilon_0 \epsilon q$ is the screened Coulomb interaction in a dual-gated setup whose gate distance is $d_\perp \sim 10$ nm [76]. Here ϵ is the dielectric constant and ϵ_0 is the vacuum permittivity. The density operator $\rho(\boldsymbol{q}) = \sum_{n,n'} \sum_{\boldsymbol{k},\boldsymbol{k}'} \sum_\tau \Lambda^{(\tau)}_{n,n'}(\boldsymbol{k}, \boldsymbol{k}', \boldsymbol{q}) c^\dagger_{n,\boldsymbol{k},\tau} c_{n',\boldsymbol{k}',\tau}$ where the form factor $\Lambda^{(\tau)}_{n,n'}(\boldsymbol{k}, \boldsymbol{k}', \boldsymbol{q}) = \langle \psi_{n,\boldsymbol{k},\tau} | e^{i\boldsymbol{q}\cdot\boldsymbol{r}} | \psi_{n',\boldsymbol{k}',\tau} \rangle$.

The interacting Hamiltonian Eq. (7) can be solved self-consistently by using the standard Hartree-Fock approximation [83]. To identify the CCI at $\nu = 1$ and QVSHI at $\nu = 2$ in the AB-stacked $MoTe_2/WSe_2$, we calculate the Hall conductance G_H and the spin Hall conductance G_{SH} as a function of ϵ under the electric field $E_\perp = 0.69$ V/nm at which the CCI was observed in the experiment [76]. At $\nu = 1$, the Hall

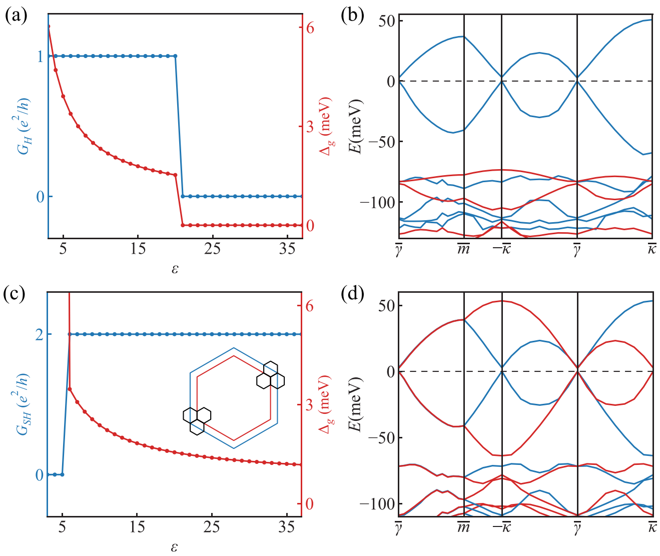

FIG. 4. (a) Hall conductance and band gap of the AB-stacked $MoTe_2/WSe_2$ heterobilayer at $\nu = 1$ and under $E_\perp = 0.69$ V/nm as a function of ϵ. (b) The corresponding energy bands given by the Hartree-Fock approximation for $\epsilon = 8$. The blue and red bands are from the $\pm$K valleys and the chemical potential is set at zero energy. Besides replacing the Hall conductance by the spin Hall conductance, (c) and (d) display the same as those in (a) and (b) at $\nu = 2$. The moiré minibands are plotted in the common MBZ of $MoTe_2/WSe_2$ represented by the black hexagon in the inset of (c).

conductance drops from e^2/h to 0 at $\epsilon \sim 21$, as shown in Fig. 4(a). When $\epsilon < 21$, the system becomes a valley-polarized CCI whose energy bands are shown in Fig. 4(b). Here the blue and red bands are from the $\pm$K valleys, respectively, and the top valence band from the +K valley with $C_+ = -1$ is empty [91]. The energy gap Δ_g decreases with ϵ and vanishes with G_H at $\epsilon \sim 21$ above which the valley polarization disappears and the system becomes a normal metal. The energy gap for $\epsilon = 8$ in Fig. 4(b) is $\Delta_g = 2.71$ meV that agrees well with the experimental data ~2.5 meV extracted from the capacitance measurement [76]. At $\nu = 2$, the spin Hall conductance jumps from 0 to $2e^2/h$ at $\epsilon \sim 6$ above which the system becomes a QVSHI, as shown in Figs. 4(c) and 4(d). In this case, the top valence bands from $\pm$K valleys with opposite Chern numbers $C_\pm = \mp 1$ are empty. The energy gap decreases with ϵ. The valley polarization only appears at strong interaction for $\epsilon < 6$, and the top two valence bands from either +K or −K valley are empty. Because the two bands from the same valley carry opposite Chern numbers, the system becomes a valleypolarized trivial insulator.

Discussion and summary.— The minimum requirement to realize topological minibands in our study is some nonzero Berry curvature which is due to the intrinsic Dirac structure of TMD. This is different from the other proposals that require the inclusion of interlayer tunneling [84,92] or pseudomagnetic field [93] in the TMD heterobilayer. The pseudomagnetic field is induced by the strain effect and can lead to the quantum spin Hall effect in TMD [94]. The relevance of pseudomagnetic field to the observed CCI in $MoTe_2/WSe_2$ remains unknown. For example, no strain-induced topological band is identified in the fully-relaxed large-scale DFT calculation [84]. Therefore, we neglect this effect here. In particular, we show that the topological phase, when protected by the symmetry of moiré potential, survives to arbitrarily large Dirac band gap that cannot be captured by the existing model Eq. (2). This mechanism is also verified for a different moiré potential with $\mathcal{C}_4$ symmetry that forms a square MSL [83]. Besides TMD heterobilayers, the massive DF on the surface of an axion insulator and in the bulk of a monolayer TMD can also couple to a modulating potential and give rise to topological mininbands, as explicitly elucidated in the Supplemental Material [83]. In these systems, the modulating potential can be generated by the spatially periodic modulation of magnetic proximity coupling and dielectric screening [95].

In summary, we spotlight the topological flat minibands that can emerge from the massive DF confined in a moiré potential. The topological phase is enabled by the Dirac structure and can be protected by the symmetry of moiré potential, which provides a paradigm to study the interplay between electric correlation and nontrivial topology. We take the $MoTe_2/WSe_2$ heterobilayer as an example and show that the CCI and QVSHI can be stabilized by the Coulomb interaction. Our work provides a mechanism to the topological states observed in the TMD heterobilayer and points a direction to design topological moiré materials.

Acknowledgments.—The work done at LANL was carried out under the auspices of the U.S. DOE NNSA under Contract No. 89233218CNA000001 through the LDRD Program. S.Z.L. was also supported by the U.S. Department of Energy, Office of Science, Basic Energy Sciences, Materials Sciences and Engineering Division, Condensed Matter Theory Program. The work at the University of Texas at Dallas is supported by the Air Force Office of Scientific Research (FA9550-20-1-0220), National Science Foundation (PHY-2110212), and Army Research Office (W911NF-17-1-0128). H.L. and K.S. acknowledge support through NSF Grant No. NSF-EFMA-1741618.

[1] A. H. Castro Neto, F. Guinea, N. M. R. Peres, K. S. Novoselov, and A. K. Geim, The electronic properties of graphene, Rev. Mod. Phys. **81**, 109 (2009).

[2] K. F. Mak, C. Lee, J. Hone, J. Shan, and T. F. Heinz, Atomically Thin MoS_2: A New Direct-Gap Semiconductor, Phys. Rev. Lett. **105**, 136805 (2010).

[3] D. Xiao, G.-B. Liu, W. Feng, X. Xu, and W. Yao, Coupled Spin and Valley Physics in Monolayers of MoS_2 and Other Group-VI Dichalcogenides, Phys. Rev. Lett. **108**, 196802 (2012).

[4] M. Katsnelson, K. Novoselov, and A. Geim, Chiral tunnelling and the Klein paradox in graphene, Nat. Phys. **2**, 620 (2006).

[5] D. Xiao, W. Yao, and Q. Niu, Valley-Contrasting Physics in Graphene: Magnetic Moment and Topological Transport, Phys. Rev. Lett. **99**, 236809 (2007).

[6] K. F. Mak, K. L. McGill, J. Park, and P. L. McEuen, The valley Hall effect in MoS_2 transistors, Science **344**, 1489 (2014).

[7] W. Yao, D. Xiao, and Q. Niu, Valley-dependent optoelectronics from inversion symmetry breaking, Phys. Rev. B **77**, 235406 (2008).

[8] T. Cao, G. Wang, W. Han, H. Ye, C. Zhu, J. Shi, Q. Niu, P. Tan, E. Wang, B. Liu *et al.*, Valley-selective circular dichroism of monolayer molybdenum disulphide, Nat. Commun. **3**, 887 (2012).

[9] A. L. Sharpe, E. J. Fox, A. W. Barnard, J. Finney, K. Watanabe, T. Taniguchi, M. A. Kastner, and D. Goldhaber-Gordon, Emergent ferromagnetism near three-quarters filling in twisted bilayer graphene, Science **365**, 605 (2019).

[10] Y.-H. Zhang, D. Mao, Y. Cao, P. Jarillo-Herrero, and T. Senthil, Nearly flat Chern bands in moiré superlattices, Phys. Rev. B **99**, 075127 (2019).

[11] Z. Song, Z. Wang, W. Shi, G. Li, C. Fang, and B. A. Bernevig, All Magic Angles in Twisted Bilayer Graphene are Topological, Phys. Rev. Lett. **123**, 036401 (2019).

[12] Y.-H. Zhang, D. Mao, and T. Senthil, Twisted bilayer graphene aligned with hexagonal boron nitride: Anomalous Hall effect and a lattice model, Phys. Rev. Research **1**, 033126 (2019).

[13] J. Y. Lee, E. Khalaf, S. Liu, X. Liu, Z. Hao, P. Kim, and A. Vishwanath, Theory of correlated insulating behaviour and spin-triplet superconductivity in twisted double bilayer graphene, Nat. Commun. **10**, 1 (2019).

[14] M. Serlin, C. Tschirhart, H. Polshyn, Y. Zhang, J. Zhu, K. Watanabe, T. Taniguchi, L. Balents, and A. Young, Intrinsic quantized anomalous Hall effect in a moiré heterostructure, Science **367**, 900 (2020).

[15] P. Stepanov, M. Xie, T. Taniguchi, K. Watanabe, X. Lu, A. H. MacDonald, B. A. Bernevig, and D. K. Efetov, Competing zero-field Chern insulators in superconducting twisted bilayer graphene (2020), arXiv:2012.15126 [cond-mat.mes-hall]

[16] M. Xie and A. H. MacDonald, Nature of the Correlated Insulator States in Twisted Bilayer Graphene, Phys. Rev. Lett. **124**, 097601 (2020).

[17] N. Bultinck, S. Chatterjee, and M. P. Zaletel, Mechanism for Anomalous Hall Ferromagnetism in Twisted Bilayer Graphene, Phys. Rev. Lett. **124**, 166601 (2020).

[18] F. Wu and S. Das Sarma, Collective Excitations of Quantum Anomalous Hall Ferromagnets in Twisted Bilayer Graphene, Phys. Rev. Lett. **124**, 046403 (2020).

[19] Y. Su and S.-Z. Lin, Current-Induced Reversal of Anomalous Hall Conductance in Twisted Bilayer Graphene, Phys. Rev. Lett. **125**, 226401 (2020).

[20] K. P. Nuckolls, M. Oh, D. Wong, B. Lian, K. Watanabe, T. Taniguchi, B. A. Bernevig, and A. Yazdani, Strongly correlated Chern insulators in magic-angle twisted bilayer graphene, Nature (London) **588**, 610 (2020).

[21] Y. Choi, H. Kim, Y. Peng, A. Thomson, C. Lewandowski, R. Polski, Y. Zhang, H. S. Arora, K. Watanabe, T. Taniguchi *et al.*, Correlation-driven topological phases in magic-angle twisted bilayer graphene, Nature (London) **589**, 536 (2021).

[22] S. Wu, Z. Zhang, K. Watanabe, T. Taniguchi, and E. Y. Andrei, Chern insulators, van hove singularities and topological flat bands in magic-angle twisted bilayer graphene, Nat. Mater. **20**, 488 (2021).

[23] I. Das, X. Lu, J. Herzog-Arbeitman, Z.-D. Song, K. Watanabe, T. Taniguchi, B. A. Bernevig, and D. K. Efetov, Symmetry-broken Chern insulators and Rashba-like Landau-level crossings in magic-angle bilayer graphene, Nat. Phys. **17**, 710 (2021).

[24] J. M. Park, Y. Cao, K. Watanabe, T. Taniguchi, and P. Jarillo-Herrero, Flavour Hund's coupling, Chern gaps and charge diffusivity in moiré graphene, Nature (London) **592**, 43 (2021).

[25] Y. Wang, J. Herzog-Arbeitman, G. W. Burg, J. Zhu, K. Watanabe, T. Taniguchi, A. H. MacDonald, B. A. Bernevig, and E. Tutuc, Topological edge transport in twisted double-bilayer graphene (2021), arXiv:2101.03621 [cond-mat.mes-hall].

[26] A. T. Pierce, Y. Xie, J. M. Park, E. Khalaf, S. H. Lee, Y. Cao, D. E. Parker, P. R. Forrester, S. Chen, K. Watanabe *et al.*, Unconventional sequence of correlated Chern insulators in magic-angle twisted bilayer graphene, Nat. Phys. **17**, 1210 (2021).

[27] M. He, J. Cai, Y.-H. Zhang, Y. Liu, Y. Li, T. Taniguchi, K. Watanabe, D. H. Cobden, M. Yankowitz, and X. Xu, Chirality-dependent topological states in twisted double bilayer graphene (2021), arXiv:2109.08255 [cond-mat.mes-hall].

[28] B. L. Chittari, G. Chen, Y. Zhang, F. Wang, and J. Jung, Gate-Tunable Topological Flat Bands in Trilayer Graphene Boron-Nitride Moiré Superlattices, Phys. Rev. Lett. **122**, 016401 (2019).

[29] Y.-H. Zhang and T. Senthil, Bridging Hubbard model physics and quantum Hall physics in trilayer graphene/$h-$BN moiré superlattice, Phys. Rev. B **99**, 205150 (2019).

[30] G. Chen, A. L. Sharpe, E. J. Fox, Y.-H. Zhang, S. Wang, L. Jiang, B. Lyu, H. Li, K. Watanabe, T. Taniguchi *et al.*, Tunable correlated Chern insulator and ferromagnetism in a moiré superlattice, Nature (London) **579**, 56 (2020).

[31] F. Wu, T. Lovorn, E. Tutuc, I. Martin, and A. H. MacDonald, Topological Insulators in Twisted Transition Metal Dichalcogenide Homobilayers, Phys. Rev. Lett. **122**, 086402 (2019).

[32] Y. Cao, V. Fatemi, S. Fang, K. Watanabe, T. Taniguchi, E. Kaxiras, and P. Jarillo-Herrero, Unconventional superconductivity in magic-angle graphene superlattices, Nature (London) **556**, 43 (2018).

[33] M. Yankowitz, S. Chen, H. Polshyn, Y. Zhang, K. Watanabe, T. Taniguchi, D. Graf, A. F. Young, and C. R. Dean, Tuning superconductivity in twisted bilayer graphene, Science **363**, 1059 (2019).

[34] G. Chen, A. L. Sharpe, P. Gallagher, I. T. Rosen, E. J. Fox, L. Jiang, B. Lyu, H. Li, K. Watanabe, T. Taniguchi *et al.*, Signatures of tunable superconductivity in a trilayer graphene moiré superlattice, Nature (London) **572**, 215 (2019).

[35] X. Lu, P. Stepanov, W. Yang, M. Xie, M. A. Aamir, I. Das, C. Urgell, K. Watanabe, T. Taniguchi, G. Zhang *et al.*, Superconductors, orbital magnets and correlated states in magic-angle bilayer graphene, Nature (London) **574**, 653 (2019).

[36] P. Stepanov, I. Das, X. Lu, A. Fahimniya, K. Watanabe, T. Taniguchi, F. H. Koppens, J. Lischner, L. Levitov, and D. K. Efetov, Untying the insulating and superconducting orders in magic-angle graphene, Nature (London) **583**, 375 (2020).

[37] H. S. Arora, R. Polski, Y. Zhang, A. Thomson, Y. Choi, H. Kim, Z. Lin, I. Z. Wilson, X. Xu, J.-H. Chu *et al.*, Superconductivity in metallic twisted bilayer graphene stabilized by WSe_2, Nature (London) **583**, 379 (2020).

[38] Y. Saito, J. Ge, K. Watanabe, T. Taniguchi, and A. F. Young, Independent superconductors and correlated insulators in twisted bilayer graphene, Nat. Phys. **16**, 926 (2020).

[39] Y. Cao, D. Rodan-Legrain, J. M. Park, N. F. Yuan, K. Watanabe, T. Taniguchi, R. M. Fernandes, L. Fu, and P. Jarillo-Herrero, Nematicity and competing orders in superconducting magic-angle graphene, Science **372**, 264 (2021).

[40] J. M. Park, Y. Cao, K. Watanabe, T. Taniguchi, and P. Jarillo-Herrero, Tunable strongly coupled superconductivity in magic-angle twisted trilayer graphene, Nature (London) **590**, 249 (2021).

[41] Z. Hao, A. Zimmerman, P. Ledwith, E. Khalaf, D. H. Najafabadi, K. Watanabe, T. Taniguchi, A. Vishwanath, and P. Kim, Electric field–tunable superconductivity in alternating-twist magic-angle trilayer graphene, Science **371**, 1133 (2021).

[42] Y. Cao, J. M. Park, K. Watanabe, T. Taniguchi, and P. Jarillo-Herrero, Pauli-limit violation and re-entrant superconductivity in moiré graphene, Nature (London) **595**, 526 (2021).

[43] H. Kim, Y. Choi, C. Lewandowski, A. Thomson, Y. Zhang, R. Polski, K. Watanabe, T. Taniguchi, J. Alicea, and S. Nadj-Perge, Spectroscopic signatures of strong correlations and unconventional superconductivity in twisted trilayer graphene (2021), arXiv:2109.12127 [cond-mat.mes-hall].

[44] C. Xu and L. Balents, Topological Superconductivity in Twisted Multilayer Graphene, Phys. Rev. Lett. **121**, 087001 (2018).

[45] H. Guo, X. Zhu, S. Feng, and R. T. Scalettar, Pairing symmetry of interacting fermions on a twisted bilayer graphene superlattice, Phys. Rev. B **97**, 235453 (2018).

[46] F. Wu, A. H. MacDonald, and I. Martin, Theory of Phonon-Mediated Superconductivity in Twisted Bilayer Graphene, Phys. Rev. Lett. **121**, 257001 (2018).

[47] M. Fidrysiak, M. Zegrodnik, and J. Spałek, Unconventional topological superconductivity and phase diagram for an effective two-orbital model as applied to twisted bilayer graphene, Phys. Rev. B **98**, 085436 (2018).

[48] Y. Su and S.-Z. Lin, Pairing symmetry and spontaneous vortex-antivortex lattice in superconducting twisted-bilayer graphene: Bogoliubov-de Gennes approach, Phys. Rev. B **98**, 195101 (2018).

[49] C.-C. Liu, L.-D. Zhang, W.-Q. Chen, and F. Yang, Chiral Spin Density Wave and $d + id$ Superconductivity in the Magic-Angle-Twisted Bilayer Graphene, Phys. Rev. Lett. **121**, 217001 (2018).

[50] D. M. Kennes, J. Lischner, and C. Karrasch, Strong correlations and $d + id$ superconductivity in twisted bilayer graphene, Phys. Rev. B **98**, 241407(R) (2018).

[51] H. Isobe, N. F. Q. Yuan, and L. Fu, Unconventional Superconductivity and Density Waves in Twisted Bilayer Graphene, Phys. Rev. X **8**, 041041 (2018).

[52] B. Roy and V. Juričić, Unconventional superconductivity in nearly flat bands in twisted bilayer graphene, Phys. Rev. B **99**, 121407(R) (2019).

[53] T. Huang, L. Zhang, and T. Ma, Antiferromagnetically ordered Mott insulator and d+ id superconductivity in twisted bilayer graphene: A quantum monte carlo study, Sci. Bull. **64**, 310 (2019).

[54] S. Ray, J. Jung, and T. Das, Wannier pairs in superconducting twisted bilayer graphene and related systems, Phys. Rev. B **99**, 134515 (2019).

[55] B. Lian, Z. Wang, and B. A. Bernevig, Twisted Bilayer Graphene: A Phonon-Driven Superconductor, Phys. Rev. Lett. **122**, 257002 (2019).

[56] J. González and T. Stauber, Kohn-Luttinger Superconductivity in Twisted Bilayer Graphene, Phys. Rev. Lett. **122**, 026801 (2019).

[57] Y.-Z. You and A. Vishwanath, Superconductivity from valley fluctuations and approximate SO(4) symmetry in a weak coupling theory of twisted bilayer graphene, npj Quantum Mater. **4**, 16 (2019).

[58] T. Cea and F. Guinea, Coulomb interaction, phonons, and superconductivity in twisted bilayer graphene, Proc. Natl. Acad. Sci. **118**, e2107874118 (2021).

[59] R. M. Fernandes and L. Fu, Charge-4e Superconductivity from Multicomponent Nematic Pairing: Application to Twisted Bilayer Graphene, Phys. Rev. Lett. **127**, 047001 (2021).

[60] E. Khalaf, S. Chatterjee, N. Bultinck, M. P. Zaletel, and A. Vishwanath, Charged skyrmions and topological origin of superconductivity in magic-angle graphene, Sci. Adv. **7**, eabf5299 (2021).

[61] W. Qin and A. H. MacDonald, In-Plane Critical Magnetic Fields in Magic-Angle Twisted Trilayer Graphene, Phys. Rev. Lett. **127**, 097001 (2021).

[62] E. Lake and T. Senthil, Re-entrant superconductivity through a quantum Lifshitz transition in twisted trilayer graphene (2021), arXiv:2104.13920 [cond-mat.mes-hall].

[63] P. J. Ledwith, G. Tarnopolsky, E. Khalaf, and A. Vishwanath, Fractional Chern insulator states in twisted bilayer graphene: An analytical approach, Phys. Rev. Research **2**, 023237 (2020).

[64] C. Repellin and T. Senthil, Chern bands of twisted bilayer graphene: Fractional Chern insulators and spin phase transition, Phys. Rev. Research **2**, 023238 (2020).

[65] Z. Liu, A. Abouelkomsan, and E. J. Bergholtz, Gate-Tunable Fractional Chern Insulators in Twisted Double Bilayer Graphene, Phys. Rev. Lett. **126**, 026801 (2021).

[66] H. Li, U. Kumar, K. Sun, and S.-Z. Lin, Spontaneous fractional Chern insulators in transition metal dichalcogenide moiré superlattices, Phys. Rev. Research **3**, L032070 (2021).

[67] Y. Xie, A. T. Pierce, J. M. Park, D. E. Parker, E. Khalaf, P. Ledwith, Y. Cao, S. H. Lee, S. Chen, P. R. Forrester *et al.*, Fractional Chern insulators in magic-angle twisted bilayer graphene (2021), arXiv:2107.10854 [cond-mat.mes-hall].

[68] F. Wu, T. Lovorn, E. Tutuc, and A. H. MacDonald, Hubbard Model Physics in Transition Metal Dichalcogenide Moiré Bands, Phys. Rev. Lett. **121**, 026402 (2018).

[69] Y. Zhang, N. F. Q. Yuan, and L. Fu, Moiré quantum chemistry: Charge transfer in transition metal dichalcogenide superlattices, Phys. Rev. B **102**, 201115(R) (2020).

[70] Y. Tang, L. Li, T. Li, Y. Xu, S. Liu, K. Barmak, K. Watanabe, T. Taniguchi, A. H. MacDonald, J. Shan, and K. F. Mak, Simulation of Hubbard model physics in WSe_2/WS_2 moiré superlattices, Nature (London) **579**, 353 (2020).

[71] E. C. Regan, D. Wang, C. Jin, M. I. B. Utama, B. Gao, X. Wei, S. Zhao, W. Zhao, Z. Zhang, K. Yumigeta *et al.*, Mott and generalized wigner crystal states in WSe_2/WS_2 moiré superlattices, Nature (London) **579**, 359 (2020).

[72] Y. Xu, S. Liu, D. A. Rhodes, K. Watanabe, T. Taniguchi, J. Hone, V. Elser, K. F. Mak, and J. Shan, Correlated insulating states at fractional fillings of moiré superlattices, Nature (London) **587**, 214 (2020).

[73] Z. Chu, E. C. Regan, X. Ma, D. Wang, Z. Xu, M. I. B. Utama, K. Yumigeta, M. Blei, K. Watanabe, T. Taniguchi, S. Tongay, F. Wang, and K. Lai, Nanoscale Conductivity Imaging of Correlated Electronic States in WSe_2/WS_2 Moiré Superlattices, Phys. Rev. Lett. **125**, 186803 (2020).

[74] X. Huang, T. Wang, S. Miao, C. Wang, Z. Li, Z. Lian, T. Taniguchi, K. Watanabe, S. Okamoto, D. Xiao *et al.*, Correlated insulating states at fractional fillings of the WS_2/WSe_2 moiré lattice, Nat. Phys. **17**, 715 (2021).

[75] H. Li, S. Li, E. C. Regan, D. Wang, W. Zhao, S. Kahn, K. Yumigeta, M. Blei, T. Taniguchi, K. Watanabe *et al.*, Imaging two-dimensional generalized wigner crystals, Nature (London) **597**, 650 (2021).

[76] T. Li, S. Jiang, B. Shen, Y. Zhang, L. Li, Z. Tao, T. Devakul, K. Watanabe, T. Taniguchi, L. Fu *et al.*, Quantum anomalous Hall effect from intertwined moiré bands, Nature (London) **600**, 641 (2021).

[77] G.-B. Liu, D. Xiao, Y. Yao, X. Xu, and W. Yao, Electronic structures and theoretical modelling of two-dimensional group-VIB transition metal dichalcogenides, Chem. Soc. Rev. **44**, 2643 (2015).

[78] C. Fang, M. J. Gilbert, and B. A. Bernevig, Bulk topological invariants in noninteracting point group symmetric insulators, Phys. Rev. B **86**, 115112 (2012).

[79] F. D. M. Haldane, Model for a Quantum Hall Effect without Landau Levels: Condensed-Matter Realization of the ”Parity Anomaly”, Phys. Rev. Lett. **61**, 2015 (1988).

[80] In triangular lattice, there is one site per unit cell and the $\mathcal{PT}$ and $\mathcal{C}_3$ symmetries can not stabilize any Dirac cone because there is only one single band.

[81] L. Meckbach, J. Hader, U. Huttner, J. Neuhaus, J. T. Steiner, T. Stroucken, J. V. Moloney, and S. W. Koch, Ultrafast band-gap renormalization and build-up of optical gain in monolayer $MoTe_2$, Phys. Rev. B **101**, 075401 (2020).

[82] N. Mounet, M. Gibertini, P. Schwaller, D. Campi, A. Merkys, A. Marrazzo, T. Sohier, I. E. Castelli, A. Cepellotti, G. Pizzi, and N. Marzari, Two-dimensional materials from high-throughput computational exfoliation of experimentally known compounds, Nat. Nanotechnol. **13**, 246 (2018).

[83] See Supplemental Material at http://link.aps.org/supplemental/10.1103/PhysRevResearch.4.L032024 for (1) Wannier orbitals of moiré minibands, (2) comparison between the two continuum models in the trivial phase, (3) local stacking configurations in AA- and AB-stacked TMD heterobilayers, (4) details of Hartree-Fock calculations, (5) topological phase protected by the $\mathcal{C}_4$ symmetry of moiré potential, and (6) potential realizations of massive Dirac fermions confined in a moiré potential, which includes Refs. [31,95–101].

[84] Y. Zhang, T. Devakul, and L. Fu, Spin-textured Chern bands in Ab-stacked transition metal dichalcogenide bilayers, Proc. Natl. Acad. Sci. **118**, e2112673118 (2021).

[85] C. Zhang, C.-P. Chuu, X. Ren, M.-Y. Li, L.-J. Li, C. Jin, M.-Y. Chou, and C.-K. Shih, Interlayer couplings, Moiré patterns, and 2D electronic superlattices in MoS_2/WSe_2 hetero-bilayers, Sci. Adv. **3**, e1601459 (2017).

[86] S. Shabani, D. Halbertal, W. Wu, M. Chen, S. Liu, J. Hone, W. Yao, D. N. Basov, X. Zhu, and A. N. Pasupathy, Deep moiré potentials in twisted transition metal dichalcogenide bilayers, Nat. Phys. **17**, 720 (2021).

[87] W. T. Geng, V. Wang, Y. C. Liu, T. Ohno, and J. Nara, Moiré potential, lattice corrugation, and band gap spatial variation in a twist-free $MoTe_2/MoS_2$ heterobilayer, J. Phys. Chem. Lett. **11**, 2637 (2020).

[88] F. Wu, T. Lovorn, and A. H. MacDonald, Topological Exciton Bands in Moiré Heterojunctions, Phys. Rev. Lett. **118**, 147401 (2017).

[89] T. Li, S. Jiang, L. Li, Y. Zhang, K. Kang, J. Zhu, K. Watanabe, T. Taniguchi, D. Chowdhury, L. Fu, J. Shan, and K. F. Mak, Continuous Mott transition in semiconductor moiré superlattices, Nature (London) **597**, 350 (2021).

[90] C. Robert, R. Picard, D. Lagarde, G. Wang, J. P. Echeverry, F. Cadiz, P. Renucci, A. Högele, T. Amand, X. Marie, I. C. Gerber, and B. Urbaszek, Excitonic properties of semiconducting monolayer and bilayer $MoTe_2$, Phys. Rev. B **94**, 155425 (2016).

[91] There are two degenerate ground states with the top valence band from either the +K or −K valley is empty at $\nu = 1$.

[92] Q. Tong, H. Yu, Q. Zhu, Y. Wang, X. Xu, and W. Yao, Topological mosaics in moiré superlattices of van der Waals heterobilayers, Nat. Phys. **13**, 356 (2017).

[93] Y.-M. Xie, C.-P. Zhang, J.-X. Hu, K. F. Mak, and K. T. Law, Valley-Polarized Quantum Anomalous Hall State in Moiré $MoTe_2/WSe_2$ Heterobilayers, Phys. Rev. Lett. **128**, 026402 (2022).

[94] M. A. Cazalilla, H. Ochoa, and F. Guinea, Quantum Spin Hall Effect in Two-Dimensional Crystals of Transition-Metal Dichalcogenides, Phys. Rev. Lett. **113**, 077201 (2014).

[95] Y. Xu, C. Horn, J. Zhu, Y. Tang, L. Ma, L. Li, S. Liu, K. Watanabe, T. Taniguchi, J. C. Hone *et al.*, Creation of moiré bands in a monolayer semiconductor by spatially periodic dielectric screening, Nat. Mater. **20**, 645 (2021).

[96] M. Koshino, N. F. Q. Yuan, T. Koretsune, M. Ochi, K. Kuroki, and L. Fu, Maximally Localized Wannier Orbitals and the Extended Hubbard Model for Twisted Bilayer Graphene, Phys. Rev. X **8**, 031087 (2018).

[97] J. Kang and O. Vafek, Symmetry, Maximally Localized Wannier States, and a Low-Energy Model for Twisted Bilayer Graphene Narrow Bands, Phys. Rev. X **8**, 031088 (2018).

[98] K. Sun, W. V. Liu, A. Hemmerich, and S. D. Sarma, Topological semimetal in a fermionic optical lattice, Nat. Phys. **8**, 67 (2012).

[99] X.-L. Qi, T. L. Hughes, and S.-C. Zhang, Topological field theory of time-reversal invariant insulators, Phys. Rev. B **78**, 195424 (2008).

[100] M. Mogi, M. Kawamura, R. Yoshimi, A. Tsukazaki, Y. Kozuka, N. Shirakawa, K. Takahashi, M. Kawasaki, and Y. Tokura, A magnetic heterostructure of topological insulators as a candidate for an axion insulator, Nat. Mater. **16**, 516 (2017).

[101] D. Xiao, J. Jiang, J.-H. Shin, W. Wang, F. Wang, Y.-F. Zhao, C. Liu, W. Wu, M. H. W. Chan, N. Samarth, and C.-Z. Chang, Realization of the Axion Insulator State in Quantum Anomalous Hall Sandwich Heterostructures, Phys. Rev. Lett. **120**, 056801 (2018).